Pursuant to the DOE Public Access Plan, this document represents the authors' peer-reviewed, accepted manuscript. The published version of the article is available from the relevant publisher.

Effect of thermal annealing on the redistribution of alkali metals in $Cu(In,Ga)Se_2$ solar cells on glass substrate

Yukiko Kamikawa,[1,a)] Jiro Nishinaga,[1] Shogo Ishizuka,[1] Takeshi Tayagaki,[1]
Harvey Guthrey,[2] Hajime Shibata,[1] Koji Matsubara,[1] Shigeru Niki[1]

[1]*National Institute of Advanced Industrial Science and Technology (AIST), Tsukuba, Ibaraki 305-8568, Japan.*

[2]*National Renewable Energy Laboratory, Golden, Colorado 80401, USA*

Abstract

The precise control of alkali-metal concentrations in $Cu(In,Ga)Se_2$ (CIGS) solar cells via post deposition treatment (PDT) has recently attracted attention. When PDT is performed at an elevated temperature, an accompanying annealing effect is expected. Here, we investigate how thermal annealing affects the redistribution of alkali metals in CIGS solar cells on glass substrates and the properties of the solar cells. In addition, we investigate the origin of non-homogeneous alkali-metal depth profiles that are typical of CIGS grown using a three-stage process. In particular, we use secondary-ion mass spectrometry measurements of the ion concentration as a function of distance from the CIGS surface to investigate the impact of thermal annealing on the distribution of alkali metals (Na, Ka, and Rb) and constituent elements (Ga and In) in the CIGS absorbers. We find that the depth profiles of the alkali metals strongly reflect the density of sites that tend to accommodate alkali metals, i.e., vacancies. Annealing at elevated temperature caused a re-distribution of the alkali metals. The thermal-diffusion kinetics of alkali metals depends strongly on the species involved. We introduced low flux KF-PDT to study a side effect of KF-PDT, i.e., Na removal from CIGS, separately from its predominant effects such as surface modification. When sufficient amounts of Na are supplied

Pursuant to the DOE Public Access Plan, this document represents the authors' peer-reviewed, accepted manuscript. The published version of the article is available from the relevant publisher.

from the soda lime glass (SLG) via annealing at an elevated temperature, the negative effect was not apparent. Conversely, when the Na supply was not sufficient, it caused a deterioration of the photovoltaic properties.

[a)] Corresponding author: yukiko-kamikawa@aist.go.jp

Pursuant to the DOE Public Access Plan, this document represents the authors' peer-reviewed, accepted manuscript. The published version of the article is available from the relevant publisher.

I. INTRODUCTION

Chalcopyrite $Cu(In,Ga)Se_2$ (CIGS) solar cells have attracted attention as a promising photovoltaic technology because of their advantages such as high energy yield, low temperature coefficient of power loss, low sensitivity to shadowing, and short energy-payback time.[1] High certified conversion efficiencies of 22.6%[2,3] and 22.9%[4] have been achieved for the CIGS solar cells on glass substrates. The CIGS solar cells, which can be fabricated using thin metal films[5–7] and plastics as substrates,[8,9] also have potential for use as flexible modules and could contribute to low-cost manufacturing[1] and to an increased installation base.[10]

The incorporation of alkali metals, specifically sodium (Na), into CIGS absorbers significantly improves the properties of CIGS solar cells. For example, doping CIGS absorbers with Na improves the electronic properties of CIGS devices by increasing *p*-type conductivity and enhancing the open-circuit voltage.[11–15] In addition, Na improves the grain boundary (GB) properties, thereby enabling the fabrication of highly efficient solar cells from polycrystalline CIGS.[16] Recent reports indicate that doping with heavier alkali metals potassium (K), rubidium (Rb), and cesium (Cs) improves the properties of CIGS devices by improving the quality of *pn* junctions through modification of the CIGS-surface composition.[2,8,17] Since the distinct benefits of doping CIGS absorbers with K were reported by Chilirá et al. in 2013,[1,8] the use of post-deposition treatment (PDT) has boosted the efficiency of CIGS solar cells.[1,2,8,18] To fully exploit the desirable effects of doping by various alkali metals, several alkali-metal species are often doped into CIGS absorbers. However, the ion-exchange interactions between different alkali-metal species give rise to a complex behavior.[2,8,17,19,20] Thus, the precise control of alkali-metal concentrations in the CIGS solar cells must be mastered.

Rigid glass is one of the most widely used substrates for CIGS solar cells because it is thermally stable, it is chemically inert, and its thermal expansion coefficient is similar to that of CIGS.[1] When PDT is performed at an elevated temperature, an accompanying annealing

Pursuant to the DOE Public Access Plan, this document represents the authors' peer-reviewed, accepted manuscript. The published version of the article is available from the relevant publisher.

effect is expected. In addition, Na removal from a CIGS absorber during KF-PDT has been reported by several research groups.[2,8,17,19] Thus, understanding thermal diffusion of alkali metals from alkali-containing glass into CIGS absorbers during annealing and interaction with those supplied by PDT and controlling the resulting concentration of alkali metals in CIGS absorbers are important issues. In this paper, we comprehensively discuss how alkali metals redistribute within the CIGS absorber during annealing and how they affect the properties of solar cells fabricated therefrom. Next, we introduced low flux KF-PDT to focus on the effect of Na removal from CIGS during PDT, separately from its predominant effects such as surface modification.[2,8,17,19] These discussions are based on the results of secondary-ion mass spectroscopy (SIMS), which reveal how annealing time (0–60 min) and temperature (350–550 °C) and low flux KF-PDT affect alkali-metal redistribution in CIGS.

II. EXPERIMENT

Soda lime glass (SLG) was used as substrate. The typical alkali-metal compositions in the SLG were ~10, ~1, and <0.01 weight% for Na, K, and Rb, respectively. A 1-µm-thick Mo back contact was deposited on an SLG substrate using in-line dc sputtering with an argon back-pressure of 0.7 Pa. For the samples in section III.A, the Mo back contacts were subjected to chemical etching to remove the naturally formed oxidized layer using an alkaline solution. For the samples in section III.B, we used as-grown Mo back contacts. The CIGS absorber was grown through a three-stage process.[21] The growth temperatures were 350 °C, 550 °C, and 550 °C for the first, second, and third stages, respectively. The beam-equivalent pressure ratio of Se (P_{Se}) for group III metals ($P_{III} = P_{Ga} + P_{In}$) was set to $P_{Se}/P_{III} = 9–10$.[22] Typical Ga/III and Cu/III ratios evaluated by electron probe micro analyzer (EPMA) in the CIGS absorber are ~0.38 and ~0.93, respectively. A Cu-rich CIGS absorber was also fabricated via a modified three-stage process, where Cu was co-deposited with Ga, In, and Se in the initial part of the third stage. Immediately after the CIGS crystal growth, the samples were annealed with or

Pursuant to the DOE Public Access Plan, this document represents the authors' peer-reviewed, accepted manuscript. The published version of the article is available from the relevant publisher.

without KF irradiation at various temperatures (350–550 °C) under a Se flux in a vacuum chamber. The temperature of the KF Knudsen cell was set to 630 °C, which corresponds to a flux of ~10^{12} cm^{-2} s^{-1}. The KF flux was set below the optimum setting[23,24] to focus on the interaction between K and Na by minimizing additional K effects such as surface modification. The KF deposition time was 10 min. CIGS solar cells with as-grown absorbers were also fabricated for use as reference samples. For the reference samples, the CIGS absorbers were immediately cooled after CIGS growth. An approximately 50-nm-thick CdS buffer layer was formed by chemical-bath deposition on CIGS absorbers. Radio-frequency and dc sputtering was used to deposit 60-nm-thick ZnO and 350-nm-thick *n*-type ZnO:Al, respectively, on the CdS layer. Al electrode was deposited on the ZnO:Al layer. No antireflection coating was used. The typical cell size is ~0.5 cm^2.

We used SIMS measurements with Cs^+ as primary ion to measure concentrations of alkali metals (Na, K, and Rb) and constituent elements as a function of distance from the surface of the CIGS absorbers. Some samples were analyzed from the substrate side to minimize the knock-on effect. An EPMA was also used to determine the composition of CIGS absorbers. CdS/CIGS/Mo/SLG samples were subjected to chemical etching with HCl solution to remove the CdS layer before EPMA measurement of the CIGS surface. Some CIGS absorbers were mechanically peeled off from the Mo back electrode and evaluated from the rear surface. The space-charge density N_{CV} was evaluated using capacitance–voltage measurements[25,26] at a frequency of 10 kHz with an LCR meter (Agilent E4980A). The cross section of CIGS solar cells was studied by scanning spreading resistance microscopy (SSRM) to study the spatial distribution of resistance. Before these measurements, the cross section was mechanically polished to obtain a flat surface. SSRM was done on E-sweep (SII-NT) with a diamond-coated single-crystal Si probe.

III. RESULTS AND DISCUSSION

Pursuant to the DOE Public Access Plan, this document represents the authors' peer-reviewed, accepted manuscript. The published version of the article is available from the relevant publisher.

A. Impact of thermal annealing

We first investigated the diffusion of alkali metals in CIGS absorbers during annealing. Figure 1 shows the SIMS depth profiles of Na, K, and Rb in CIGS solar cells with the CIGS absorbers annealed at 550 °C for 20 and 60 min and the as-grown sample. The concentrations [Na] and [K] increase with increasing annealing time. Upon annealing, [Na] increases in regions II, III, and IV (0.2–2.0 μm) and slightly decreases in region I (0–0.2 μm), and [K] increases especially in regions II (0.2–0.7 μm) and IV (1.5–2.0 μm). In region III, [K] remains relatively constant. No remarkable change occurs in [Rb] upon annealing. These results reveal how redistribution varies during annealing depending on the alkali-metal species, which is likely due to different thermal equilibrium concentrations of the alkali metals, namely, [Na] > [K] > [Rb].[20]

Next, we analyze how the concentration of alkali metals as a function of depth in the CIGS absorber is affected by annealing. The concentrations [Na], [K], and [Rb] decrease with distance from the CdS side of the CIGS surface into the CIGS bulk (see regions I and II in Fig. 1). These concentrations increase upon approaching the rear surface (Mo side) from the CIGS bulk (see region IV in Fig. 1). We discuss the origin of those alkali-metal concentration gradients. The diffusion length $2\sqrt{D_{\mathrm{Na}}^{\mathrm{V}} t_{\mathrm{an}}}$ of Na is predicted to be ~5 to ~10 μm for an annealing time t_{an} = 20 and 60 min using the reported diffusion coefficient $D_{\mathrm{Na}}^{\mathrm{V}} \quad 9.7\times 10^{-9} \exp\left(-0.36\ \mathrm{eV}/k_B T\right) \mathrm{cm}^2\mathrm{s}^{-1}$.[27,28] These diffusion lengths are much greater than the CIGS thickness. Such large diffusion lengths mean that, during annealing, Na is supplied throughout the entire CIGS absorber from the SLG. Thus, we believe that the alkali-metal concentration gradients observed in Fig. 1 do not simply reflect the thermal diffusion of the alkali-metal species. Instead, those concentration profiles likely reflect the density of sites that tend to accommodate alkali metals. Vacancies (e.g., mono-vacancy V_{Cu}), di-vacancies (V_{Cu}–V_{Se}), and vacancy clusters[29] could serve as such sites. A schematic of a typical CIGS

Pursuant to the DOE Public Access Plan, this document represents the authors' peer-reviewed, accepted manuscript. The published version of the article is available from the relevant publisher.

absorber is depicted in Fig. 1 (d). Highly Cu-poor regions should include a high density of those vacancies. Grain boundaries (GBs) are known to accommodate 100 times more alkali species than the grain interior.[30] When the concentration of alkali metals would exceed its solubility limit, it would phase-separate into alkali-metal compounds,[20] and segregate at GBs. Thus, the variation in GB concentration could also affect the alkali-metal concentration profiles.

For further analysis, we evaluate the alkali-metal concentration profiles in a Cu-rich CIGS absorber. Figure 2 shows the SIMS depth profiles of Na, K, and Rb in Cu-rich (Cu/III ~1.01) and Cu-poor (Cu/III ~0.93) CIGS absorbers. No annealing was performed for those samples. The Cu-rich CIGS absorbers have a constant SIMS concentration profile for [Na], [K], and [Rb], which indicates that these alkali metals are distributed homogeneously throughout the bulk of the CIGS absorber. Because vacancies are reported to be homogeneously distributed in a Cu-rich sample,[31] the constant profiles of alkali metals could reflect the homogeneous distribution of vacancies. We thus conclude that the alkali-metal depth profiles primary reflect the distribution of vacancies in CIGS bulk and possibly the GBs. In typical Cu-poor CIGS, Cu/III near the CIGS surface is as low as 0.6 (region I in Fig. 1) as evaluated by EPMA with an acceleration voltage V_{acc} of 5 kV, which gives a penetration depth of about 0.1 μm. These results indicate that a highly Cu-poor compound forms at the CIGS surface which should include a high density of vacancies.[29,31,32] The high concentration of vacancies would lead to a deeper diffusion of vacancies into the CIGS layer (region II in Fig. 1).[29,31] At the rear surface of the CIGS layer mechanically peeled off, EPMA gives Cu/III < 0.9, which indicates that the rear surface is also highly Cu poor. In region III, EPMA gives Cu/III > 0.95. Conversely, for the Cu-rich sample, EPMA gives Cu/III > 1 throughout the regions. Although no significant difference appears in GB density (i.e., grain size) in Cu-rich samples compared with Cu-poor samples, the influence of GBs cannot be completely excluded. The reduced Cu content at the GBs may also affect the alkali-metal concentration in the GBs.

A calculation based on $CuInSe_2$ (CIS) reveals that the migration barrier for Na, K, and Rb

Pursuant to the DOE Public Access Plan, this document represents the authors' peer-reviewed, accepted manuscript. The published version of the article is available from the relevant publisher.

can be less than 0.4 eV when diffusion is combined with vacancies in Cu-poor CIS.[20] In Cu-poor CIS, Na and K prefer to fill in the pre-existing Cu vacancies, although the larger Rb and K ions (with respect to Na) tend more to phase separate into XInSe$_2$ (X= Rb, K) compounds and segregate at the GBs.[20] Na also could phase-separate into Na_2Se when the [Na] exceeds its solubility limit. To the best of our knowledge, the equilibrium concentrations of Na, K, and Rb in Cu-poor CIS have not yet been clarified. On the basis of the previous reports, the different redistribution of Na, K, and Rb during annealing shown in Fig. 1 may be explained as follows: the increased [Na] and [K] during annealing in regions II and IV in Fig. 1 may correspond to the redistribution of vacancies; Na and K would fill these vacancies. Large amounts of Na, K, and Rb should also segregate at the GBs and possibly at defects such as vacancy clusters. Unchanged [Rb] upon annealing could indicate a small equilibrium concentration in the Cu-poor CIGS bulk. Thus, the redistribution of vacancies would not significantly affect its distribution.

We next discuss how annealing affects the electrical properties of the CIGS absorber. The resistivity distribution in the CIGS absorber was evaluated using SSRM. Figure 3 shows the SSRM images for a CIGS solar cell with a nonannealed absorber [Fig. 3(a)] and with an absorber annealed at 550 °C for 20 min [Fig. 3(b)]. Both samples have a highly resistive layer on top of the CIGS layer (i.e., at the vicinity of the CdS/CIGS interface). The highly resistive layer spreads upon annealing, but more work is needed to identify the origin of this layer. It may be the layer that contains a high density of vacancies[33]. The promoted Cd doping into the CIGS layer during the growth of CdS[34,35] could be one of the possible formation mechanisms for the highly resistive layer. Cd doping improves the hetero-interfaces.[8] In fact, as per light IV curves, the external collection efficiencies of the two samples shown in Fig. 3 do not differ significantly. Further experiments are needed to determine how the presence of a highly resistive layer and its thickness influence the photovoltaic properties of the solar cell.

We now turn to an explanation of how annealing affects the fraction of constituent

Pursuant to the DOE Public Access Plan, this document represents the authors' peer-reviewed, accepted manuscript. The published version of the article is available from the relevant publisher.

elements as a function of distance from the CIGS absorber surface. Figure 4(a) shows the Ga/III ratio in the CIGS solar cells as a function of distance from the CdS/CIGS interface upon annealing at 550 °C for 60 min and for an as-grown sample. Figure 4(a) shows that the Ga gradient in the annealed CIGS absorber is small compared with the as-grown sample. This result is attributed to elemental interdiffusion during annealing. Figure 4(b) shows the external quantum efficiency (EQE) for the CIGS solar cells with absorbers annealed at 550 °C for 60 min and that for the as-grown CIGS absorber. The absorption edge blueshifts in the solar cell with annealed absorbers, which is consistent with the smaller Ga gradient upon annealing. The minimum Ga/III ratio increases in the annealed cells, resulting in an increased minimum bandgap energy E_g.[36] The discrepancy in the SIMS concentration profiles of Se and Cu between samples remains within the measurement error.

Figure 5 shows the solar-cell characteristics obtained from the current–voltage curves from the CIGS solar cells with absorbers annealed at 550 °C for 20, 45, and 60 min and from as-grown samples. Each group of samples comprises eight devices. Figure 5(a) shows that conversion efficiency decreases with the annealing. Figure 5(b) shows that the open-circuit voltage V_{OC} decreases significantly with increasing annealing time. The reduction in V_{OC} is expected to be the primary cause of the reduced efficiency. The deficit in V_{OC} (i.e., $E_g/q - V_{OC}$) is also shown in Fig. 5(c): it increases with increasing annealing time. The E_g was estimated from the absorption edge of the EQE spectrum. Figures 5(d) and5(e) show that the short-circuit current and fill factor also decrease with annealing time but are secondary causes. Figure 5(f) shows the space-charge density N_{CV} and the space-charge width W calculated from capacitance–voltage measurements: N_{CV} decreases and W increases with increasing annealing time. The reduced acceptor density in the CIGS absorbers should be the primary cause of the decrease in V_{OC}. Although, we have not yet fully clarified the cause of this variation in the N_{CV}, we consider that the N_{CV} variation can be attributed to elemental interdiffusion of In and Ga during annealing as discussed in Fig. 4 (a). The migrated element could occupy a V_{Cu} site and

Pursuant to the DOE Public Access Plan, this document represents the authors' peer-reviewed, accepted manuscript. The published version of the article is available from the relevant publisher.

then create defect levels such as In_{Cu} donor levels.[37,38] Even though the Na substitution of In_{Cu} to from inert Na_{Cu} has been reported to be exothermic,[15] the formation of In_{Cu} could occur in the grain interior of CIGS, where [Na] might be lower than V_{Cu} concentration.

B. Impact of annealing temperature during KF-PDT

Next, we varied the annealing temperature and studied the effect on the alkali-metal redistribution. Figure 6 shows the concentrations [Na], [K], and [Rb] measured by SIMS as a function of distance from the CIGS surface in a CIGS solar cell with an absorber annealed at 350 °C and 550 °C for 20 min and in an as-grown sample. The concentrations [Na], [K], and [Rb] remain almost constant upon annealing at 350 °C, which likely indicates a decrease in thermal diffusion with decreasing annealing temperature. The SIMS profiles shown in Fig. 6 differ from those shown in Fig.1, that is, [Na] and [K] increase in region II due to the redistribution of vacancies caused by the thermal annealing in Fig. 1; however, regions corresponding to region II are not seen in Fig. 6. This difference can be attributed to the different V_{Cu} mobilities in those samples, which are likely due to the different Na concentrations in the grain interiors of the CIGS samples. Figures 1 and 6 show the SIMS profiles in the different samples. In the samples discussed in Fig. 1, naturally formed oxidized layers on the Mo back contacts were removed via chemical etching prior to CIGS growth. Conversely, the samples discussed in Fig. 6 were grown on unetched Mo. The distribution of Na in the CIGS varies depending on the Mo surface condition because Na is supplied from the SLG through Mo. The higher [Na] in the CIGS grain interior could reduce the V_{Cu} concentration by forming Na_{Cu}. Therefore, the mobility of V_{Cu} could be reduced because the migration of V_{Cu} is Cu migration in the opposite direction via V_{Cu} sites.

Next, we focus on the thermal diffusion of alkali metals during KF-PDT. The KF flux was set below the optimum condition[23,24] to focus on the interaction between K and Na by minimizing additional K effects such as surface modification. Figure 7 shows [Na] as a function

Pursuant to the DOE Public Access Plan, this document represents the authors' peer-reviewed, accepted manuscript. The published version of the article is available from the relevant publisher.

of distance from the CIGS surface as measured by SIMS in CIGS solar cells with absorbers annealed for 20 min at 350 °C and 550 °C. In addition, the figure compares CIGS solar cells with absorbers annealed with low flux KF irradiation and without KF irradiation. At 350 °C, [Na] decreases throughout the CIGS absorber when low flux KF-PDT is used, which indicates that Na ions are removed from the CIGS absorber during the KF-PDT. The ion-exchange interaction between Na and K is a possible mechanism for the removal of Na from the CIGS layer. Na in the Cu site (Na_{Cu}) is ejected by K, which results in the formation of K_{Cu}.[20] Another possible mechanism is that Na dissolves in the K–Se liquid phase that forms at the CIGS surface.[39] Conversely, after KF-PDT at 550 °C, [Na] is comparable to that of the sample without KF-PDT. These results show that the removal of Na during KF-PDT is partly compensated when the annealing temperature is as high as 550 °C.

Next, we discuss the solar-cell properties. Figure 8(a) shows typical current-density–voltage curves measured under white-light irradiation (~100 mW/cm^2) for CIGS solar cells with absorbers annealed at 350 °C and 550 °C. These figures compare CIGS solar cells with absorbers annealed with low flux KF irradiation and without KF irradiation. The solar-cell parameters of these solar cells are summarized in Table I. The open-circuit voltage V_{OC} = 0.67 V for the CIGS solar cell with an absorber annealed at 350 °C with low flux KF irradiation was obtained, which is significantly less than that of the CIGS solar cell with an absorber annealed at the same temperature but without KF irradiation (V_{OC} = 0.74 V). This result indicates that applying low flux KF-PDT at 350 °C reduces V_{OC} by 70 mV under the growth conditions used for this work. Conversely, the samples with absorbers annealed at 550 °C have the same V_{OC} (0.74 V) independent of KF irradiation. Figure 8(b) shows the current-density–voltage curves measured in the dark. The diode parameters obtained by a fit using the single-diode model[40] are listed in Table I. The reverse saturation current J_0 increases for the CIGS solar cell with an absorber annealed at 350 °C and with low flux KF-PDT, which cause a decrease in V_{OC}. Figure 8(c) shows the current density measured under illumination with J_{SC} subtracted off (i.e., J −

Pursuant to the DOE Public Access Plan, this document represents the authors' peer-reviewed, accepted manuscript. The published version of the article is available from the relevant publisher.

J_{SC}) as a function of applied bias voltage. The fits by the single-diode model are also shown in the figure. The curve for $J - J_{SC}$ versus V is not well reproduced by the simple single-diode model. In particular, the curve for the CIGS solar cell with an absorber annealed at 350 °C with low flux KF irradiation deviate significantly in the bias-voltage range 0–0.5 V, which indicates a reduced external collection efficiency $\eta(V)$ with forward bias.[25] The removal of Na from the front surface of CIGS might increase defect levels such as In_{Cu} and Ga_{Cu} in the region.

Figures 9 summarizes the conversion efficiency, V_{OC}, J_{SC}, and the fill factor for a CIGS solar cell with absorbers annealed at temperatures ranging from 350 °C to 550 °C with low flux KF irradiation and without KF irradiation. Each sample group comprises eight solar-cell devices. The solar cells with an absorber annealed at 350 °C with low flux KF-PDT exhibit remarkably lower V_{OC} than the CIGS solar cells with an absorber annealed at higher temperatures (400–550 °C). The reduction in V_{OC} shown in Fig. 9(b) is the primary cause of the reduced efficiency. In addition, solar cells with absorbers annealed at 350 °C with low flux KF-PDT have the lowest fill factors, which is likely due to reduced external collection efficiency, as shown in Fig. 8(c). Because the variation in J_{SC} is within the measurement error, it is not the main factor causing the variation in efficiency.

Figure 10(a) shows N_{CV} for the CIGS solar cell with absorbers annealed at various annealing temperatures and with low flux KF irradiation and without KF irradiation. The reference data for our typical optimized PDT processes[23,24] are also plotted in the figure. The as-grown CIGS solar cell and the solar cell with an absorber annealed at 350 °C exhibit low carrier concentrations of $N_{CV} \sim 2 \times 10^{15}$ cm^{-3}, which is less than that for the as-grown reference discussed in section III.A. The difference is attributed to the different Mo surface conditions of the samples, as mentioned above. The N_{CV} value for the as-grown sample with chemically treated Mo was 6×10^{15}cm^{-3}, which is comparable to that discussed in section III.A. The high amount of Na in the CIGS grain interior of the sample could reduce the V_{Cu} concentration by forming Na_{Cu}.

Pursuant to the DOE Public Access Plan, this document represents the authors' peer-reviewed, accepted manuscript. The published version of the article is available from the relevant publisher.

The sample with an absorber annealed at 450 °C has $N_{CV} \sim 10^{16}$ cm^{-3}. N_{CV} decreases upon thermal annealing at higher temperatures (500–550 °C). The reduction in N_{CV} results in a reduced V_{OC}, as depicted in Fig. 9(b). Introduction of low flux of KF-PDT also reduces N_{CV}, as shown in Fig. 10(a). A remarkably low N_{CV} of ~7 × 10^{14} cm^{-3} occurs for the solar cell with an absorber annealed at 350 °C and with low flux of KF-PDT. The reduction in Na concentration shown in Fig. 7 could reduce the beneficial effect of increased acceptor density provided by Na such as reduction of In_{Cu} defect.[13,15,19] Figure 10(b) summarizes V_{OC} as a function of N_{CV}. The relationship between V_{OC} and the acceptor density N_A for an ideal *pn* homo-junction can be described as[41]

$$V_{OC} = \frac{k_B T}{q} \ln\left(\frac{J_L}{J_0} + 1\right) \approx \frac{k_B T}{q} \ln\left(\frac{J_L}{J_0}\right), \quad (1)$$

$$J_0 = q\left(\frac{D_n}{L_n} n_{po} + \frac{D_p}{L_p} p_{no}\right) \approx \sqrt{\frac{q k_B T \mu_e}{\tau_n}} n_{po} = \frac{n_i^2}{N_A} \sqrt{\frac{q k_B T \mu_e}{\tau_n}}, \quad (2)$$

where k_B, T, q, J_L, (n_{p0}, p_{n0}), (L_n, L_p), (D_n, D_p), μ_e, and τ_n are the Boltzmann constant, temperature, elementary charge, photogeneration current density, minority-carrier densities, diffusion lengths, diffusion coefficients, electron mobility, and minority-carrier lifetime, respectively. Here, we assume that $D_p p_{n0}/L_p$ is negligible because of the much lower minority-carrier density p_{n0} in wide-gap *n*-type materials (CdS) than that (n_{p0}) in *p*-type CIGS. The n_{p0} is derived from n_i^2/N_A, where n_i is an intrinsic career density. N_A is the accepter density of the CIGS.

If τ_n and μ_e remains unchanged in equation (2), the increase in N_A by an order of magnitude should result in an increase in V_{OC}: $\Delta V_{OC} \approx (k_B T/q) \ln(N_{A2}/N_{A1}) \approx 60$ mV. However, our typical samples showed a trend of ΔV_{OC} ~30 mV with one order of increase in N_{CV}. There are several possible reasons for the discrepancy. One possibility is that the N_{CV} is highly affected by density of deep levels; thus, the increase in N_A is lower than that measured

Pursuant to the DOE Public Access Plan, this document represents the authors' peer-reviewed, accepted manuscript. The published version of the article is available from the relevant publisher.

as the change in N_{CV}. Other possibility is that τ_n is reduced in the sample with high N_{CV}. The solid line in Fig. 10(b) plots our empirical V_{OC} line. A reference as a high N_{CV} sample (Ref. [23]) is also plotted in the figure.

Note that the experimental V_{OC} value in the cell with an absorber annealed at 350 °C and with low flux KF-PDT is significantly less than the empirical V_{OC} line. This indicates that an additional mechanism lies behind the decrease in open-circuit voltage in the cell. The reduced external collection efficiency shown in Fig. 9(c) is thought to be the additional loss.

Finally, we discuss the impact of thermal annealing and low flux KF-PDT. On the basis of the SIMS profiles of concentration as a function of depth in the CIGS layer, the redistribution with annealing depends on the particular alkali-metal species. The depth profiles of Na and K vary with thermal annealing at high temperatures of ~550 °C, which should be due to redistribution of the sites that tend to accommodate those alkali metals. The redistribution of these sites is accompanied by the redistribution of constituent elements of CIGS absorbers. Therefore, the N_{CV} decreased with annealing. One of the possible mechanisms is the creation of anti-site defects at that high temperature.

A side effect of KF-PDT, i.e., Na removal from CIGS was observed with low-flux KF-PDT. When sufficient amounts of Na are supplied from the SLG via annealing at an elevated temperature, the negative effect of Na removal was not apparent. Conversely, when the Na supply was not sufficient, it caused deterioration of the photovoltaic properties. Because Na is the key impurity to increase acceptor density, the removal of Na could lead to a significant reduction in acceptor density, which, in turn, degrades the photovoltaic properties, especially V_{OC}. The formation of anti-site defects is a possible mechanism that would explain this phenomenon of not only decreasing the acceptor density but also degrading the external collection efficiency. These results indicate that the supply of an adequate amount of Na could fully exploit the desirable benefit of KF-PDT even for a solar cell fabricated on a SLG substrate. The intentional addition of Na along with KF-PDT[23] is a possibility.

Pursuant to the DOE Public Access Plan, this document represents the authors' peer-reviewed, accepted manuscript. The published version of the article is available from the relevant publisher.

IV. SUMMARY

In this paper, we comprehensively discussed how thermal annealing affects the redistribution of alkali metals in CIGS during annealing and interacts with the alkali metals supplied by PDT. In addition, we investigated the origin of non-homogeneous alkali-metal depth profiles typical of CIGS grown using a three-stage process. The depth profile of alkali metals strongly reflects the density of sites that tend to accommodate alkali metals, i.e., vacancies. We also revealed that annealing at high temperature (550°C) redistributes vacancies and accordingly redistributes the alkali metals, therefore modulating the electrical properties of the CIGS.

Low flux KF-PDT was introduced to study its side effect, i.e., Na removal from CIGS, separately from its predominant effects such as surface modification. When sufficient amounts of Na are supplied from the SLG via annealing at an elevated temperature, the negative effect of Na removal was not apparent. Conversely, when the Na supply was not sufficient, it caused a deterioration of the photovoltaic properties. The undesirable removal of Na leads to a significant reduction in acceptor density and degrades the external collection efficiency. These results indicate that a supply of adequate amounts of Na to compensate the undesirable removal of Na caused by KF-PDT could fully exploit the desirable benefit of KF-PDT even for solar cells fabricated on soda lime glass substrates.

ACKNOWLEDGMENTS

This work was supported by the New Energy and Industrial Technology Development Organization (NEDO) under the Ministry of Economy, Trade and Industry (METI) of Japan. The authors would like to thank H. Takahashi, M. Iioka, and H. Higuchi for their help with the

Pursuant to the DOE Public Access Plan, this document represents the authors' peer-reviewed, accepted manuscript. The published version of the article is available from the relevant publisher.

experiments and technical support. The authors also thank T. Koida, T. Nagai, S. Kim, and H. Tampo for the fruitful discussions and continuous encouragement.

Pursuant to the DOE Public Access Plan, this document represents the authors' peer-reviewed, accepted manuscript. The published version of the article is available from the relevant publisher.

Table I. Solar-cell parameters for the CIGS solar cells with absorbers annealed at 350 °C and 550 °C with low flux KF irradiation and without KF addition and the as-grown CIGS solar cell. The diode parameters obtained by fitting dark *J–V* curves are also listed. T_{an} is the annealing temperature, *Eff.* is the solar-cell conversion efficiency, R_{sh} is the shunt resistance, R_s is the series resistance, J_0 is the reverse saturation current density, and *m* is the ideality factor.

Sample No	T_{an} (°C)	Low flux KF-PDT	*Eff.* (%)	V_{OC} (V)	J_{SC} (mA/cm^2)	*FF*	R_{sh} (kΩ)	R_{ser} (Ω·cm^2)	J_0 (×10^{-11} A/cm^2)	*m*
SQ3221-8	As grown	Without	18.0	0.72	32.0	0.78	11.6	0.51	2.77	1.36
SQ3223-8	350	Without	17.9	0.74	30.7	0.79	10.9	0.34	0.93	1.32
SQ3229-8	350	With	15.3	0.67	31.3	0.73	9.4	0.71	6.59	1.35
SQ3225-8	550	Without	17.9	0.74	31.2	0.78	12.4	0.44	2.61	1.37
SQ3228-8	550	With	18.1	0.74	31.2	0.78	7.6	0.35	1.73	1.36

Pursuant to the DOE Public Access Plan, this document represents the authors' peer-reviewed, accepted manuscript. The published version of the article is available from the relevant publisher.

Figure captions

FIG. 1. Concentration of elemental (a) Na, (b) K, and (c) Rb as a function of distance from the $Cu(In,Ga)Se_2$ (CIGS)–CdS interface in the CIGS solar cells with absorbers annealed at 550 °C for 20 and 60 min and for the as-grown CIGS solar cells. The solar cells were analyzed by secondary-ion mass spectroscopy (SIMS) from the CdS side. (d) Schematic of a typical CIGS absorber.

FIG. 2. Concentration of elemental (a) Na, (b) K, and (c) Rb as a function of distance from the CIGS–CdS interface in the CIGS solar cells with slightly Cu-rich (Cu/III ~1.01) or Cu-poor (Cu/III ~0.93) absorbers. No annealing was performed for those samples. The solar cells were analyzed by SIMS from the soda lime glass substrate side.

FIG. 3. Scanning spreading resistance microscopy images for (a) the as-grown CIGS solar cell and (b) the CIGS solar cell with an absorber annealed at 550 °C for 20 min. Both samples have a highly resistive region at the CIGS surface (i.e., in the vicinity of the CdS/CIGS interface).

FIG. 4. (a) Ratio of [Ga]/([In] + [Ga]) in CIGS solar cells with absorbers annealed at 550 °C for 60 min and for the as-grown CIGS sample. (b) External quantum efficiency for CIGS solar cells from panel (a) as a function of irradiation wavelength.

FIG. 5. (a) Conversion efficiency, (b) open-circuit voltage (V_{OC}), (c) V_{OC} deficit ($E_g/q - V_{OC}$), (d) short-circuit current density, and (e) fill factor for the CIGS solar cells with absorbers annealed at 550 °C for 20, 45, and 60 min and for the as-grown sample. (f) Space charge density and space-charge width calculated from capacitance–voltage measurements plotted as a function of annealing time.

Pursuant to the DOE Public Access Plan, this document represents the authors' peer-reviewed, accepted manuscript. The published version of the article is available from the relevant publisher.

FIG. 6. SIMS depth profiles of (a) Na, (b) K, and (c) Rb in the CIGS solar cells with absorbers annealed at 350 °C and 550 °C for 20 min and an as-grown sample.

FIG. 7. SIMS depth profiles of Na in the CIGS solar cells with absorbers annealed at 350 °C and 550 °C for 20 min. The annealings were performed with low flux KF-PDT or without KF irradiation.

FIG. 8. Current-density–voltage curves measured (a) under white-light irradiation (~100 mW/cm^2) and (b) in the dark for the CIGS solar cells with absorbers annealed at 350 °C and 550 °C with low flux KF irradiation (dashed lines) and without (solid lines) KF addition. (c) Current density measured under illumination subtracted by the J_{SC} value ($J - J_{SC}$) plotted as a function of applied bias voltage for the sample with annealing at 350 °C with low flux KF irradiation (open circles) or without (crosses) KF irradiation. The fittings by single-diode models are also shown with solid lines.

FIG. 9. Box plots of (a) efficiency, (b) open-circuit voltage, (c) current density, and (d) fill factor for CIGS solar cells with absorbers annealed at temperature ranging from 350 °C to 550 °C. Each panel compares CIGS solar cells with absorbers annealed with low flux KF irradiation and without KF addition.

FIG. 10. (a) Space-charge density as a function of annealing temperature of an absorber in CIGS solar cell with and without KF-PDT. The reference data for our typical optimized PDT processes[23,24] are also plotted in the figure. (b) Open-circuit voltage as a function of space-charge density for CIGS solar cells from the panel (a). The solid line is our empirical line. A reference as high N_{CV} sample[23] is also plotted in the figure.

Pursuant to the DOE Public Access Plan, this document represents the authors' peer-reviewed, accepted manuscript. The published version of the article is available from the relevant publisher.

References

1 T. Feurer, P. Reinhard, E. Avancini, B. Bisset, J. Löckinger, P. Fuchs, R. Carron, T. P. Weiss, J. Perrenoud, S. Stutterheim, S. Buecheler, and A. N. Tiwari, Prog. Photovoltaics **25**, 645 (2017).

2 P. Jackson, R. Wuerz, D. Hariskos, E. Lotter, W. Witte, and M. Powalla, Phys. Status. Solidi RRL **10**, 583 (2016).

3 M. A. Green, Y. Hishikawa, W. Warta, E. D. Dunlop, D. H. Levi, J. Hohl-Ebinger, and A. W. H. Ho-Baillie, Prog. Photovoltaics **25**, 668 (2017).

4 Solar Frontier Press Release:http://www.solar-frontier.com/eng/news/2017/1220_press.html

5 R. Wuerz, A. Eicke, M. Frankenfeld, F. Kessler, M. Powalla, P. Rogin, and O. Yazdani-Assl, Thin Solid Films **517**, 2415 (2009).

6 K. Moriwaki, M. Nomoto, S. Ishizuka, A. Mukai, K. Sato, H. Kobayashi, and S. Niki, Sol. Energy Mater. Sol. Cells **133**, 21 (2015).

7 P. Blösch, F. Pianezzi, A. Chirilă, P. Rossbach, S. Nishiwaki, S. Buecheler, and A. N. Tiwari, J. Appl. Phys. **113**, 54506 (2013).

8 A. Chirilă, P. Reinhard, F. Pianezzi, P. Bloesch, A. R. Uhl, C. Fella, L. Kranz, D. Keller, C. Gretener, H. Hagendorfer, D. Jaeger, R. Erni, S. Nishiwaki, S. Buecheler, and A. N. Tiwari, Nature Mater. **12**, 1107 (2013).

9 D. Rudmann, D. Bŕmaud, H. Zogg, and A. N. Tiwari, J. Appl. Phys. **97**, 84903 (2005).

10 M. Tripathy, P. K. Sadhu, and S. K. Panda, Renew. Sustain. Energy Rev. **61**, 451 (2016).

11 J. Hedström, H. Ohlsen, M. Bodegard, A. Kylner, L. Stolt, D. Hariskos, M. Ruchk, and H. W. Shock, Conference Record of the 23rd IEEE Photovoltaic Specialists Conference, Louisville (IEEE, New York, 1993), pp. 364–371.

12 M. Ruckh, D. Schmid, M. Kaiser, R. Schäffler, T. Walter, and H. M. Schock, Conference Record of the 1st World Conference on Photovoltaic Energy Conversion, Waikoloa (IEEE, New York, 1994), pp. 156–159.

Pursuant to the DOE Public Access Plan, this document represents the authors' peer-reviewed, accepted manuscript. The published version of the article is available from the relevant publisher.

13 M. A. Contreras, B. Egaas, P. Dippo, J. Webb, J. Granata, K. Ramanathan, S. Asher, A. Swartzlander, and R. Noufi, Conference Record of the 26th IEEE Photovoltaic Specialists Conference, Anaheim (IEEE, New York, 1997), pp. 359–362.

14 B. L. Kronik, D. Cahen, and H. W. Schock, Adv. Mater. **10**, 31 (1998).

15 S. Wei, S. B. Zhang, and A. Zunger, J. Appl. Phys. **85**, 7214 (1999).

16 C-Y. Liu, Z-M. Li, H-Y. Gu, S-Y. Chen, H. Xiang, and X-G. Gong, Adv. Energy Mater. **7**, 1601457 (2017).

17 P. Reinhard, B. Bissig, F. Pianezzi, E. Avancini, H. Hagendorfer, D. Keller, P. Fuchs, M. Döbeli, C. Vigo, P. Crivelli, S. Nishiwaki, S. Buecheler, and A. N. Tiwari, Chem. Mater. **27**, 5755 (2015).

18 T. Kato, Jpn. J. Appl. Phys. **56**, 04CA02 (2017).

19 F. Pianezzi, P. Reinhard, A. Chirilă, B. Bissig, S. Nishiwaki, S. Buecheler, and A. N. Tiwari, Phys. Chem. Chem. Phys. **16**, 8843 (2014).

20 M. Malitckaya, H.-P. Komsa, V. Havu, and M. J. Puska, J. Phys. Chem. C **121**, 15516 (2017).

21 A. M. Gabor, J. R. Tuttle, D. S. Albin, M. A. Contreras, R. Noufi, and A. M. Hermann, Appl. Phys. Lett. **65**, 198 (1994).

22 S. Ishizuka, A. Yamada, P. Fons, and S. Niki, Prog. Photovoltaics Res. Appl. **21**, 544 (2013).

23 J. Nishinaga, T. Koida, S. Ishizuka, Y. Kamikawa, H. Takahashi, M. Iioka, H. Higuchi, Y. Ueno, H. Shibata, and S. Niki, Appl. Phys. Express **10**, 92301 (2017).

24 Y. Kamikawa, J. Nishinaga, S. Ishizuka, H. Shibata, and S. Niki, Jpn. J. Appl. Phys. **55**, 22304 (2016).

25 R. Scheer, H-W. Shock, *Chalcogenide Photovoltaics* (Wiley-VCH, Weinheim, 2011), pp.107-108.

26 T. Eisenbarth, T. Unold, R. Caballero, C. A. Kaufmann, and H-W. Shock, J. Appl. Phys. **107**, 034509 (2010).

27 A. Laemmle, R. Wuerz, T. Schwarz, O. Cojocaru-mirédin, P. Choi, and M. Powalla, J. Appl.

Pursuant to the DOE Public Access Plan, this document represents the authors' peer-reviewed, accepted manuscript. The published version of the article is available from the relevant publisher.

Phys. **115**, 154501 (2014).

28 H. Mehrer, *Diffuion in Solids* (Springer, Berlin, 2007), pp568-575.

29 A. Uedono, M. M. Islam, T. Sakurai, C. Hugenschmidt, W. Egger, R. Scheer, Krause-R, R. Ehberg, and K. Akimoto, Thin Solid Films **603**, 418 (2016).

30 O. Cojocaru-Mirédin, P-P. Choi, D. Abou-Ras, IEEE Journal of Photovoltaics **1**, 207 (2011).

31 M. M. Islam, A. Uedono, S. Ishibashi, K. Tenjinbayashi, T. Sakurai, A. Yamada, S. Ishizuka, K. Matsubara, S. Niki, and K. Akimoto, Appl. Phys. Lett. **98**, 112105 (2011).

32 T. Maeda, W. Gong, T. Wada, Jpn. J. Appl. Phys. **55**, 04ES15 (2016).

33 T. Nishimura, S. Toki, H. Sugiura, K. Nakada, A. Yamada, Prog. Photovoltaics, in press.

34 M. Contreras, M. J. Romero, B. To, F. Hasoon, R. Noufi, S. Ward, K. Ramanathan, Thin Solid Films **403-404**, 204 (2002).

35 K. Ramanathan, F. S. Hasoon, S. Smith, D. L. Young, M. A. Contreras, P. K. Johnson, A. O. Pudov, J. R. Sites, J. Phys. Chem. Solids **64**, 1495 (2003).

36 S. H. Han, F. S. Hasoon, J. W. Pankow, A. M. Hermann, and D. H. Levi, Appl. Phys. Lett. **87**, 151904 (2005).

37 C. Persson, Y-J. Zhao, S. Lany, A. Zunger, Phys. Rev. B **72**, 035211 (2005).

38 S. B. Zhang, S-H. Wei, A. Zunger, H. Katayama-Yoshida, Phys. Rev. B **57**, 9642 (1998).

39 T. Maeda, A. Kawabata, T. Wada, Jpn. J. Appl. Phys. **54**, 08KS20 (2015).

40 Y. Kamikawa-Shimizu, H. Komaki, A. Yamada, S. Ishizuka, M. Iioka, H. Higuchi, M. Takano, K. Matsubara, H. Shibata, and S. Niki, Appl. Phys. Express **6**, 112303 (2013).

41 S. M. Sze, *Physics of Semiconductor Devices*, (Wiley, New York, 1981), pp793-798.

Pursuant to the DOE Public Access Plan, this document represents the authors' peer-reviewed, accepted manuscript. The published version of the article is available from the relevant publisher.

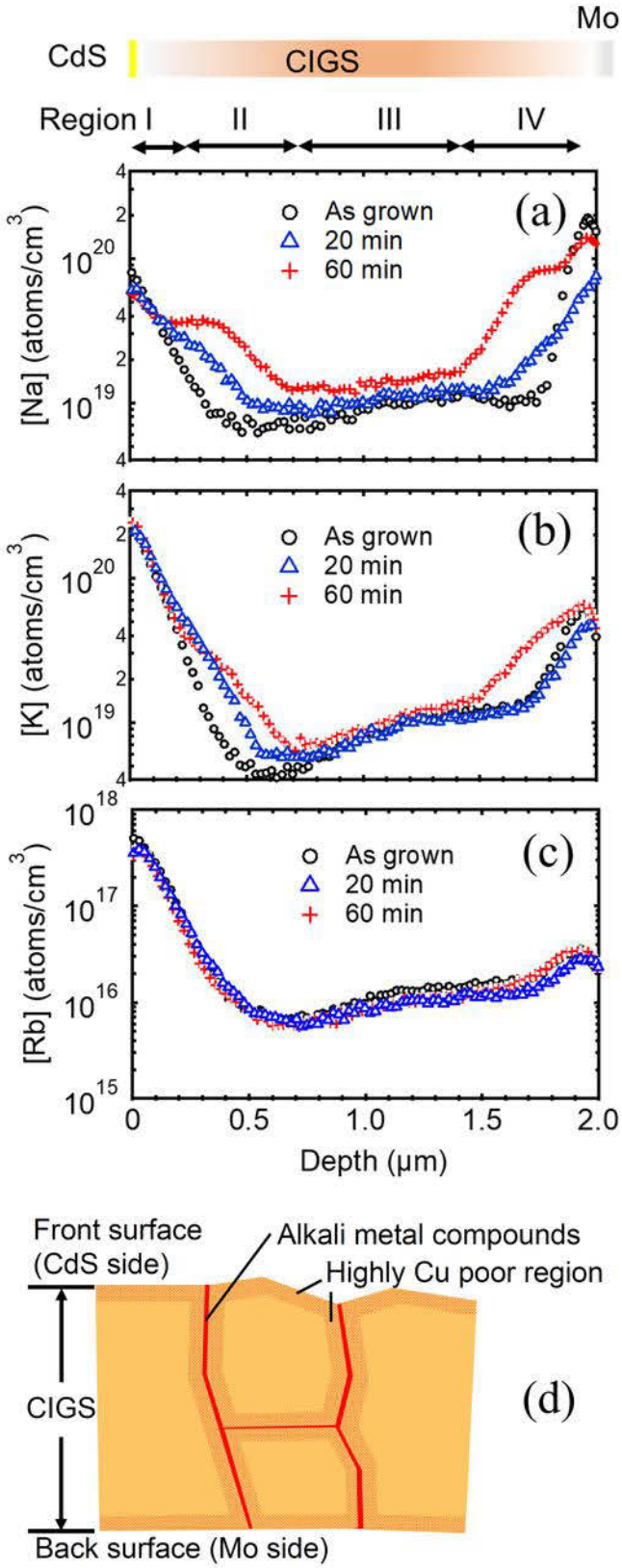

Figure 1

Y. Kamikawa et. al. Journal of Applied Physics (2017)

Pursuant to the DOE Public Access Plan, this document represents the authors' peer-reviewed, accepted manuscript. The published version of the article is available from the relevant publisher.

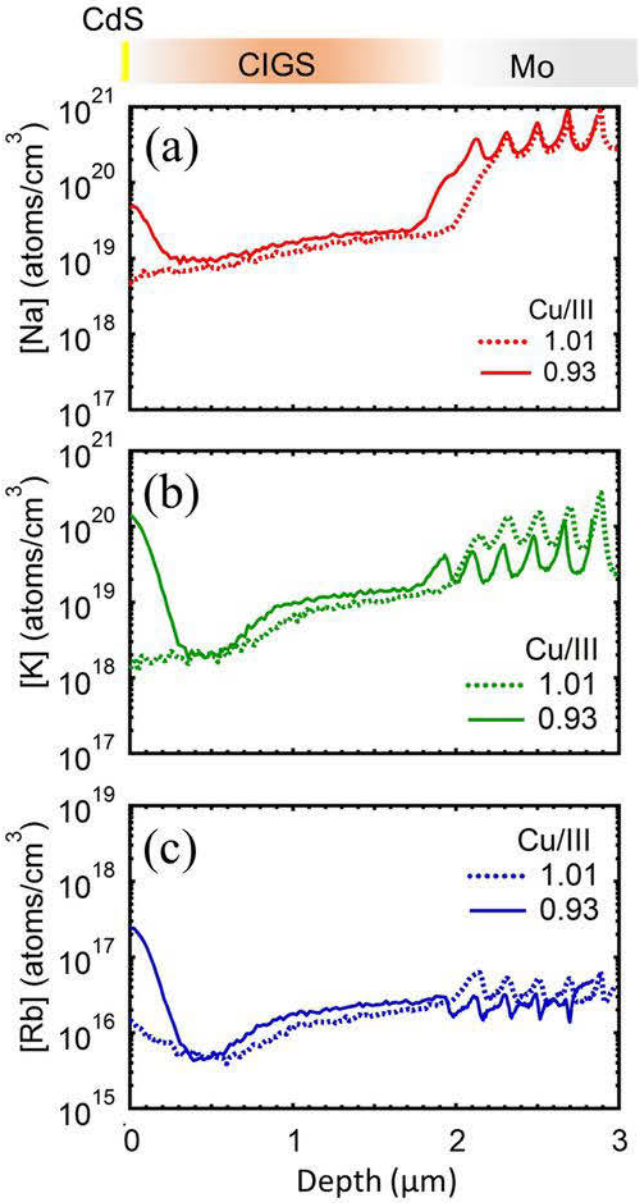

Figure 2

Pursuant to the DOE Public Access Plan, this document represents the authors' peer-reviewed, accepted manuscript. The published version of the article is available from the relevant publisher.

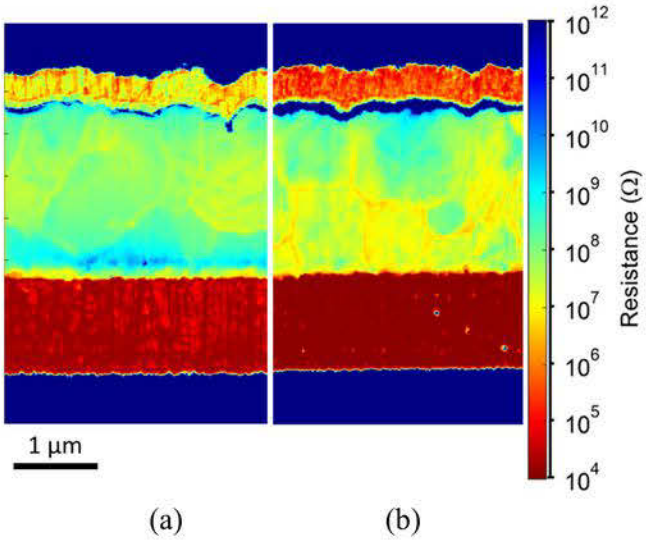

Figure 3

Pursuant to the DOE Public Access Plan, this document represents the authors' peer-reviewed, accepted manuscript. The published version of the article is available from the relevant publisher.

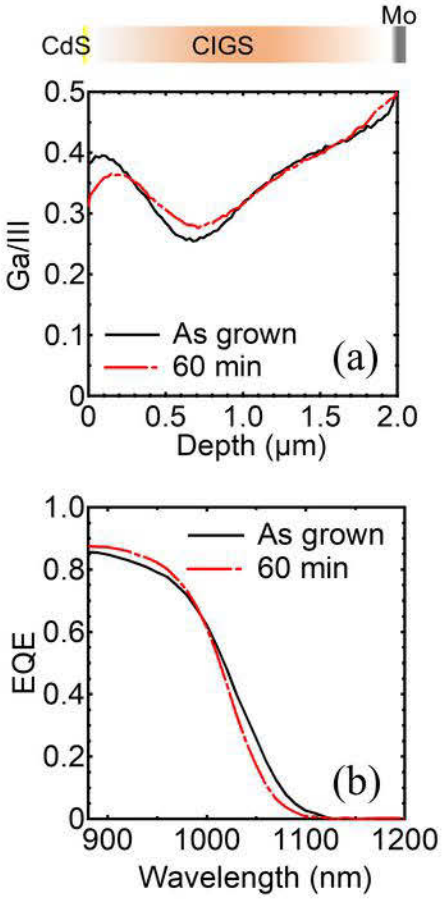

Figure 4

Y. Kamikawa et. al. Journal of Applied Physics (2017)

Pursuant to the DOE Public Access Plan, this document represents the authors' peer-reviewed, accepted manuscript. The published version of the article is available from the relevant publisher.

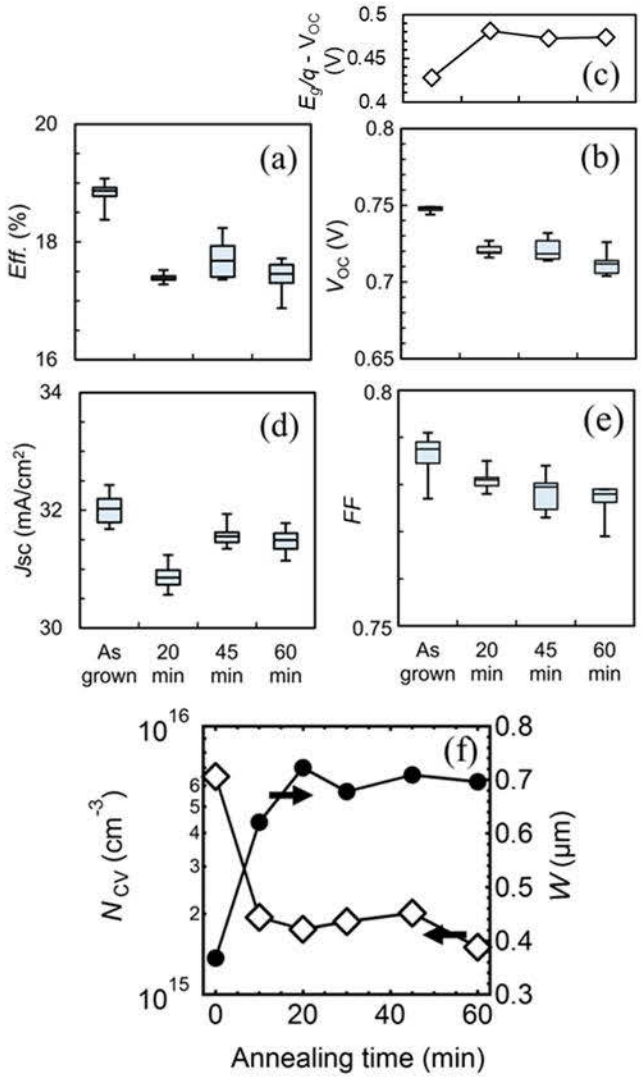

Figure 5

Pursuant to the DOE Public Access Plan, this document represents the authors' peer-reviewed, accepted manuscript. The published version of the article is available from the relevant publisher.

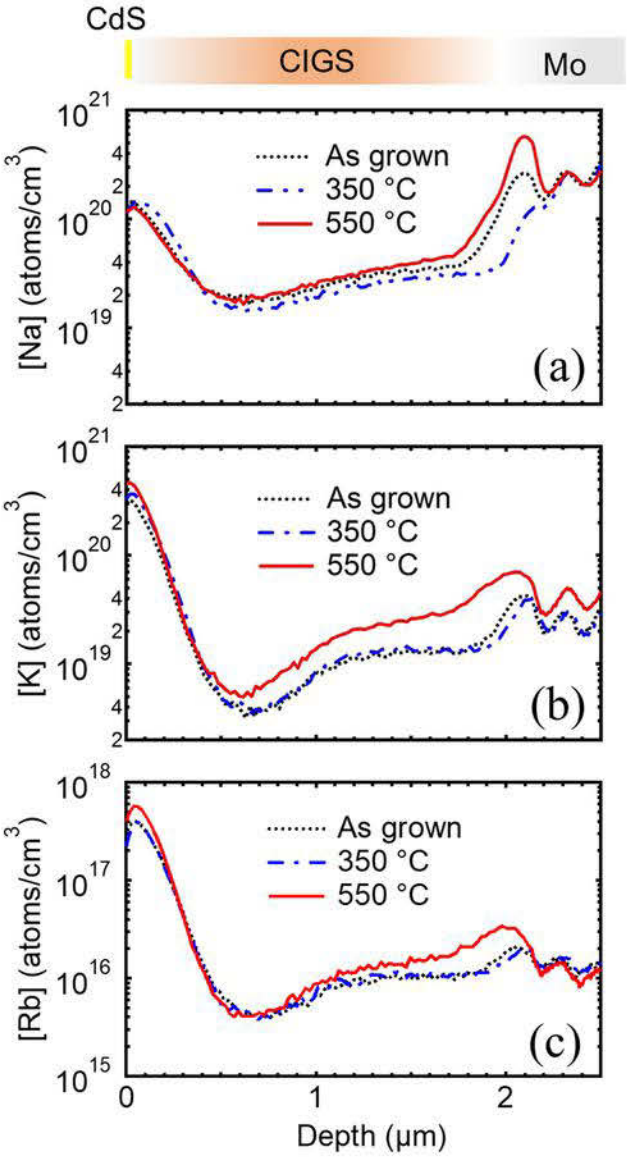

Figure 6

Pursuant to the DOE Public Access Plan, this document represents the authors' peer-reviewed, accepted manuscript. The published version of the article is available from the relevant publisher.

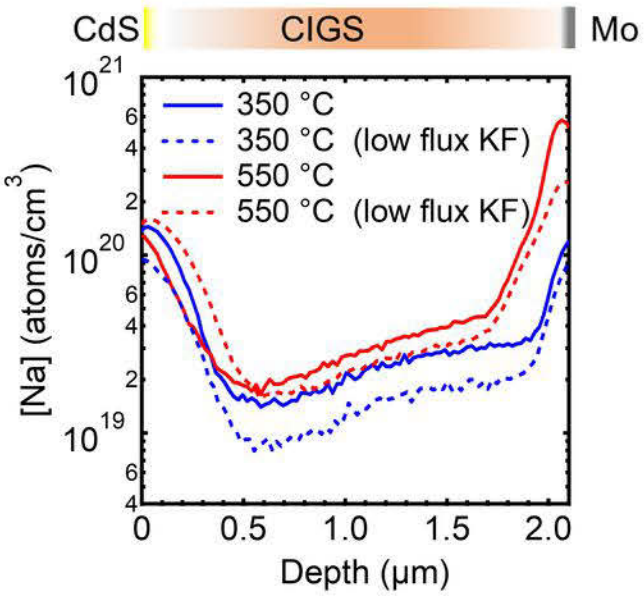

Figure 7

Pursuant to the DOE Public Access Plan, this document represents the authors' peer-reviewed, accepted manuscript. The published version of the article is available from the relevant publisher.

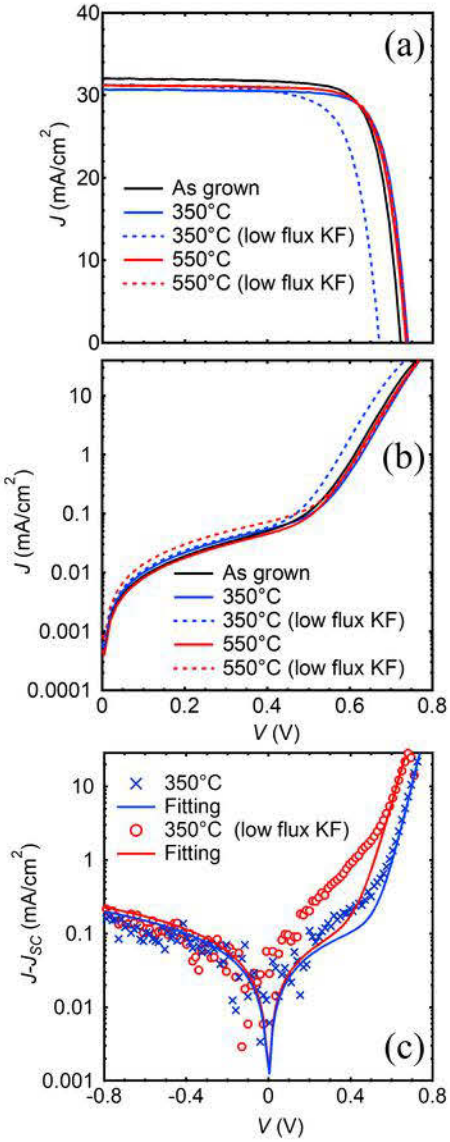

Figure 8

Pursuant to the DOE Public Access Plan, this document represents the authors' peer-reviewed, accepted manuscript. The published version of the article is available from the relevant publisher.

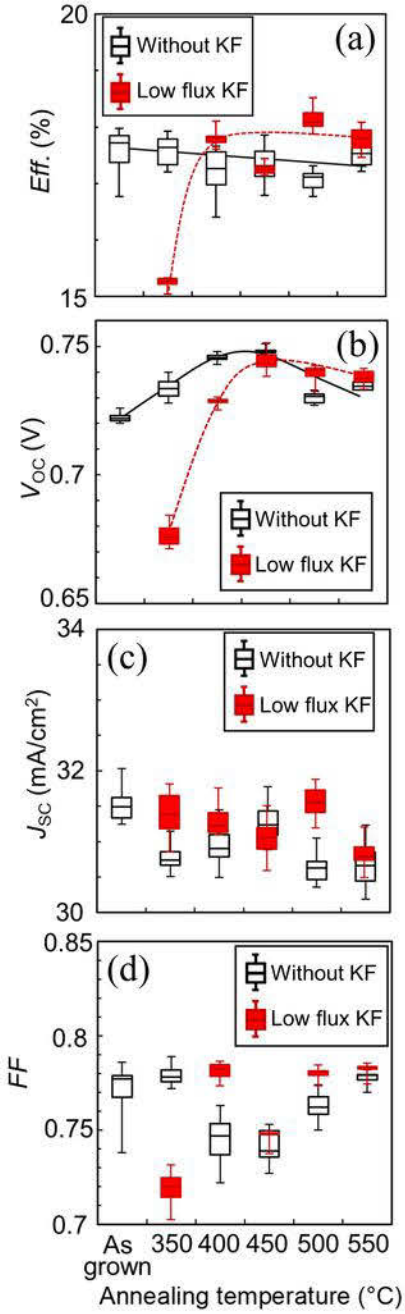

Figure 9

Y. Kamikawa et. al. Journal of Applied Physics (2017)

Pursuant to the DOE Public Access Plan, this document represents the authors' peer-reviewed, accepted manuscript. The published version of the article is available from the relevant publisher.

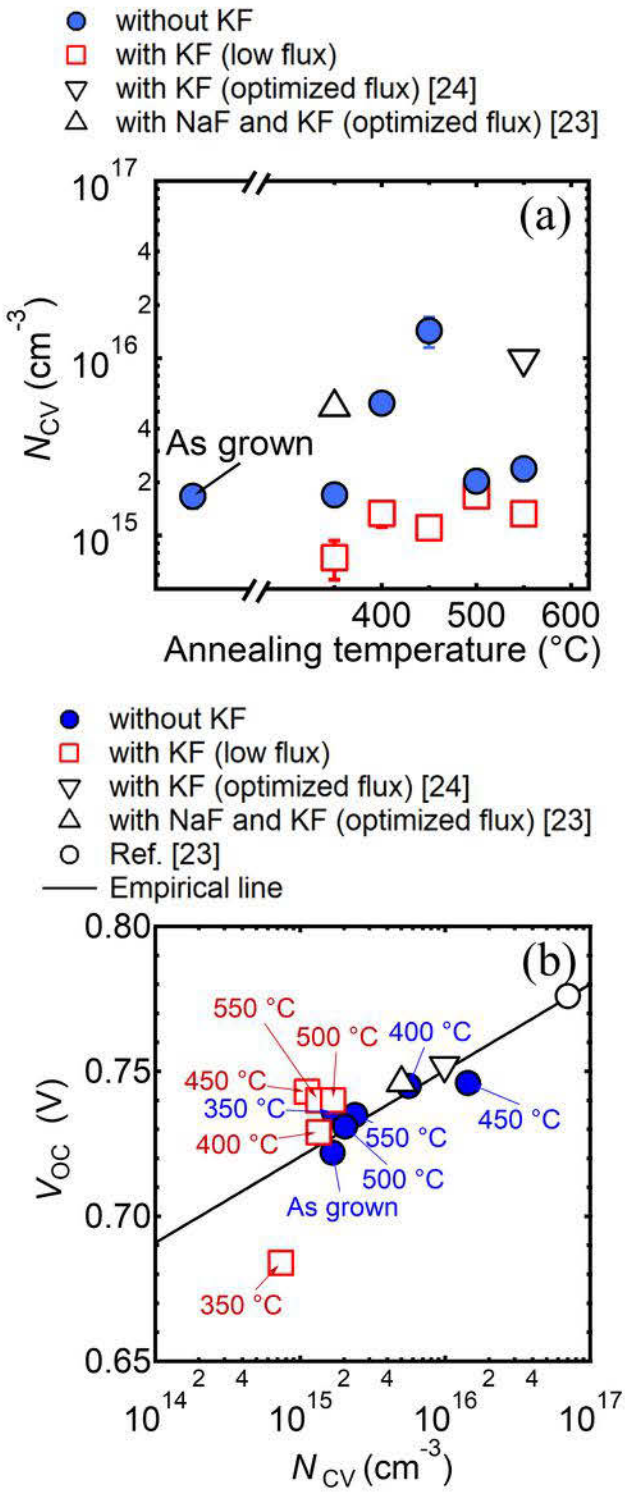

Figure 10